Noname manuscript No.
(will be inserted by the editor)

Statistical analysis of the intermediate filament network in cells of mesenchymal lineage by greyvalue-oriented image segmentation

Sebastian Lück · Alois Fichtl · Michaela Sailer · Helga Joos · Rolf E. Brenner · Paul Walther · Volker Schmidt

Received: date / Accepted: date

Abstract Intermediate filament networks are part of the cytoskeleton and protect cellular integrity during large deformations. In cells from mesenchymal lineage the cytoskeleton is centrally involved in signal transduction, thereby influencing differentiation. We study the ultrastructure of IF networks in three human mesenchymal cell types, namely undifferentiated mesenchymal stem cells, chondrocytes, and osteoblasts. In order to capture the high morphological variability of IF networks we apply techniques from image analysis to extract the network graph from 2D scanning electron microscopy (SEM) images in a fully automatic way, which allows for a high-throughput analysis of SEM data. The extracted network graphs are analyzed by techniques from spatial statistics to detect differences in network morphology between different cell types and infer strategies of network remodeling used by the cells to adapt their mechanical properties during migration and differentiation.

Keywords cytoskeleton · intermediate filaments · image analysis · spatial statistics · cell mechanics · high-throughput microscopy · mesenchymal stem cell · osteoblast · chondrocyte

This work was funded by a grant from Deutsche Forschungsgemeinschaft (SFB 518 project B21).

S. Lück · A. Fichtl · V. Schmidt
Institute of Stochastics, Ulm University, D-89069 Ulm, Germany
Tel.: +49 731 502 3531
Fax: +49 731 502 3649
E-mail: sebastian.lueck@uni-ulm.de

Michaela Sailer · Paul Walther
Electron Microscopy Facility, Ulm University, D-89069 Ulm, Germany

Rolf E. Brenner · Helga Joos
Division for Biochemistry of Joint and Connective Tissue Diseases, Department of Orthopaedics, Ulm University, D-89081 Ulm, Germany

1 Introduction

In cellular biology it is of broad interest to study morphological and this means spatial properties of cells. In this context data is naturally obtained by microscopy and often shows a high degree of biological variability. The analysis of such images can be achieved by a combination of methods from spatial statistics with techniques from image analysis which allow for an automatic extraction of relevant information. This way, datasets can be analyzed without the bias introduced by manual segmentation and with the efficiency necessary for a high-throughput microscopy adequately capturing biological variability (Weichsel et al. 2010).
In this study we analyze the morphology of the intermediate filament (IF) network in different cell types from mesenchymal origin, namely undifferentiated mesenchymal stem cells (MSC), chondrocytes (CH), i.e. cartilage forming cells, and osteoblasts (OB), i.e. bone cells. MSCs, which in literature are also termed multipotent mesenchymal stromal cells, are nonhematopoietic progenitor cells with the potential to differentiate along various mesenchymal lineages including CHs and OBs. In all of these cell types IFs are an abundant part of the cytoskeleton, which apart from the IFs is composed of the actin network and the system of microtubuli. In mesenchymal cells IFs are primarily composed of the protein vimentin and exhibit a diameter of $8 - 12nm$ (Mücke et al. 2005). In cells from mesenchymal lineage the cytoskeleton is centrally involved in transmitting signals from extracellular topographic cues and mechanical forces to the nucleus, thereby influencing cellular differentiation and function. In addition, the cytoskeleton is described to play a pivotal role in cell migration (O'Neill 2009). Though most studies on the role of the cytoskeleton during the differentiation of mesenchymal cells have so far focused on the role of actin microfilaments (Darling et al. 2008, Docheva 2008, Rodríguez et al. 2004, Treiser et al. 2010, Yourek et al. 2007), also the IF protein vimentin is involved in migration as well as in signal transduction, e.g. in chondrogenic differentiation (Bobick et al. 2010, Eriksson et al. 2009). Furthermore, the IF network responds dynamically to mechanical loading of osteoblastic cells and codetermines the viscoelastic properties of chondrocytes (Jackson et al. 2008, Trickey et al. 2004).
Vimentin IFs exhibit interesting viscoelastic properties, setting them apart from actin filaments and microtubules. They are less rigid than actin and very extensible but show a dramatic stress-stiffening at high strains, transferring from a linear to a non-linear response to increases in shear stress (Janmey et al. 1991, Kreplak et al. 2005, Lin et al. 2010). IF networks are thus well-suited to protect cellular integrity at large scale mechanic deformations, where the actin networks suffers disruption (Beil et al. 2003, Yourek et al. 2007). The viscoelastic properties of IF and other semiflexible polymer-networks are governed by their morphological properties (Heussinger and Frey 2007, Huisman et al. 2007, Lin et al. 2010, MacKintosh et al. 1995). Due to the non-linear relationship between the mean edge length of the network graph and the elastic shear modulus of the network (Lin et al. 2010, MacKintosh et al. 1995),

even small alterations in network morphology can substantially influence cell mechanics. For vimentin networks this has been recently demonstrated in an *in vitro* study by Lin et al. (2010) revealing that divalent cations crosslink filament tail-domains and thus stiffen vimentin networks. Global features of the cytoskeleton such as the gross amount of proteins and their intracellular spatial distribution may be determined by light microscopy and can be valuable sources of information (Docheva et al. 2008, Rodríguez et al. 2004, Weichsel et al. 2010). However, due to the non-linear impact of network ultrastructure on the elasticity of semiflexible polymer networks (Heussinger and Frey 2007, Huisman et al. 2007, Lin et al. 2010, MacKintosh et al. 1995) it is of great interest to investigate the morphology of the cytoskeleton at high resolution, thus analyzing network architecture at the level of single filaments and their cross-links. There is a variety of electron microscopical techniques for the visualization IF networks at this level of resolution (Sailer et al. 2010). A superior contrast of the IFs is provided by scanning electron microscopy (SEM) images of detergent extracted samples where most of the cellular structures are removed and the IFs remain surrounded by vacuum. Due to the resulting reduction in cellular complexity and the high filament contrast these images are well-suited for an automatic extraction of the network graph (Sailer et al. 2010). Since IF networks are 3D structures the most accurate assessment of network architecture can be obtained by electron tomographic 3D data (Lück et al. 2010). Nevertheless, 2D geometric network characteristics still contain the major part of morphological information since the orientation of most filaments is close to parallel to the imaging plane. Moreover, data acquisition for 3D-tomograms of IF networks as conducted in Lück et al. (2010) is extremely time-consuming. Thus, 2D methods are favorable for high-throughput studies of network morphology capturing the high variability of IF networks that is frequently found even within single biological scenarios.

In this study we introduce an image segmentation method for the analysis of 2D SEM images of IF networks, which extends previous approaches by Beil et al. (2005) in such a way that also SEM images of multi-layered networks can be analyzed, where the filamentous phase is characterized by a drastic variation of the greyvalues with decreasing IF contrast in lower network layers (Fig. 1). This technique is applied to automatically extract network graphs from a large number of SEM images recorded from cells of mesenchymal lineage. We statistically compare network morphology between different cell types and, as an important functional aspect, illustrate the impact of morphological differences on cell mechanics. Our findings indicate a distinct reorganization of the vimentin network in the cell periphery during differentiation of mesenchymal stem cells into cartilage (CH) and bone (OB) cells. This suggests that the elasticity differences between OB and CH cells measured by atomic force microscopy, which primarily resolves the actin cytoskeleton (Darling et al. 2008, Yourek et al. 2007), are accompanied by corresponding structural changes of the vimentin network, which modify the response of the cell to large scale deformations. We will further demonstrate, that there is large variability in network ultrastructure even within a single biological scenario which can be

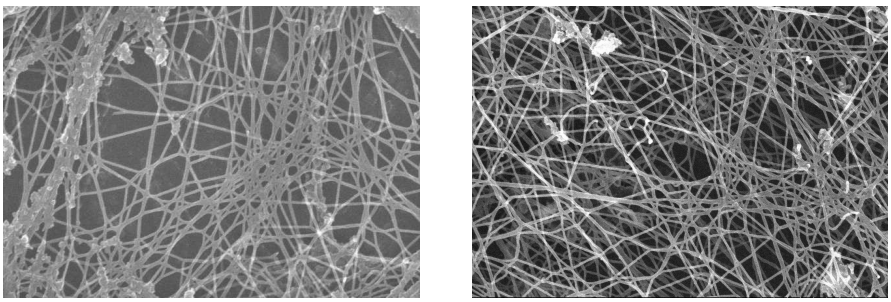

(a) (b)

Fig. 1 Scanning electron microscopy images of IF networks in a detergent extracted chondrocyte (cell periphery) (a) and an osteoblast (perinuclear compartment) (b)

linked to the regulation of cellular elasticity. In particular, variations in cross-linking and corresponding changes in the edge length distribution as reported by Lin et al. (2010) for *in vitro* polymerized vimentin networks can also be observed in our cellular image data.

2 Image acquisition and segmentation

Cells were isolated from human tissue and bone marrow as available due to standard surgical procedures. Informed consent of the patients was obtained according to the terms of the Ethics Committee of Ulm University. CHs were derived from macroscopically normal regions of cartilage harvested during knee joint replacement due to osteoarthritis. The detailed protocols used for isolation of MSCs, OBs, and CHs are described in Fiedler et al. 2002, Mayr-Wohlfart et al. 2002, and Joos et al. 2008, respectively. Early stage CHs were used after 5 days of cultivation while late stage CHs were subcultivated to passage 4. Cells were seeded on saphir discs (2500 cells/cm^2). After 2 days of adherence cells were detergent-extracted such that apart from the IF cytoskeleton cellular structures were entirely removed. Imaging by scanning electron microscopy and previous preparation steps were conducted as described in Lück et al. (2010) and further discussed in Sailer et al. (2010) (magnification $40,000$, accelerating voltage between 5 and $10kV$).

Several techniques from image analysis were combined in order to extract the graph structure of the IF network from the SEM images as vector data, i.e., as a set of line segments and their cross-links. A primary challenge for the segmentation of the SEM images was the multi-level structure of the network, leading to difficulties in the assessment of network connectivity and the separation of superposed network edges. The varying greyscale of filament pixels, which were rather bright in the top layer and substantially darker for the background filaments, required the use of greyscale-oriented methods for the

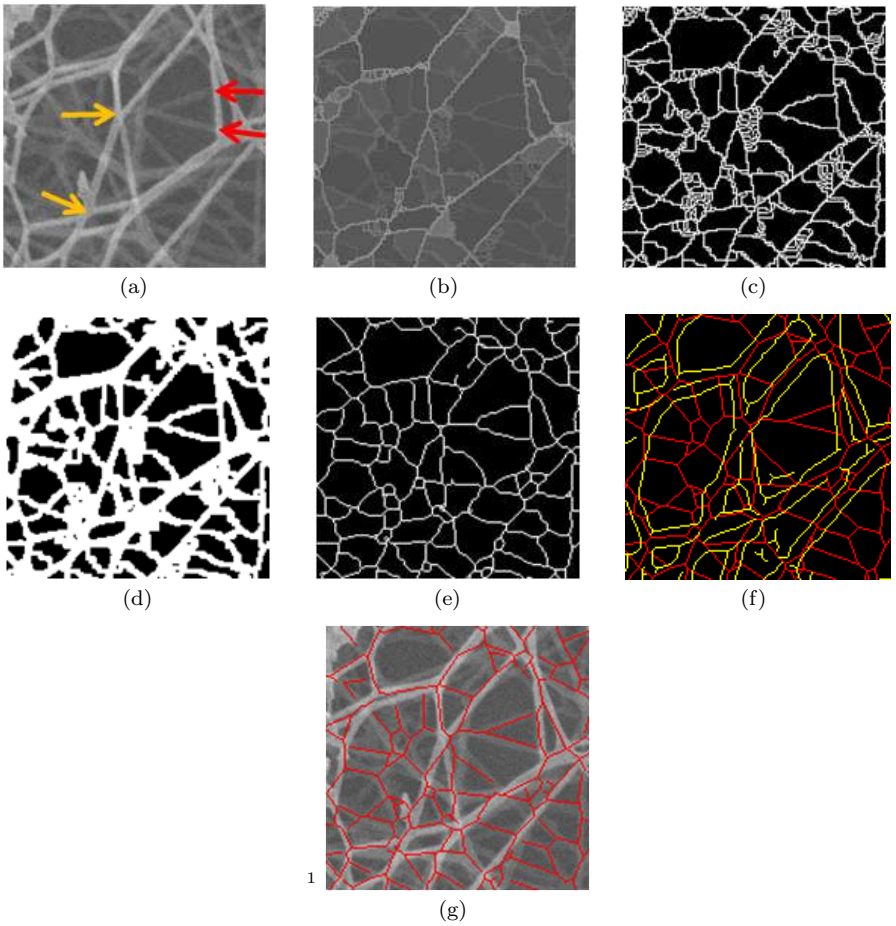

Fig. 2 Extraction of the network graph from a 2D SEM image for a small cutout of the observation window. (a) Original image, orange arrows depict real cross-links of the network, whereas the red arrows point at filaments whose trajectories are crossing each other in the 2D images without presumable contact in 3D. (b) Lower λ-leveling kernel. (c) Extracted crest lines. (d) Superposition of dilated crest lines and intermode threshold of (a). (e) Skeleton of (d). In (b) and (c) oversegmentation occurs as a consequence of local minima in upper network levels. In (d) the corresponding small network meshes are filled and thus not conserved in the final skeleton (e). (f) Red lines correspond to the skeleton in (e), whereas yellow lines mark high image gradients along filament edges. (g) Filament trajectories crossing high gradients along filament edges are interrupted and pseudo cross-links removed.

identification of the filamentous phase, which could rarely be extracted by a simple threshold-based binarization.

2.1 Lower λ-leveling kernel

In order to account for the different grey-levels of filaments in the fore- and background we implemented an algorithm for the computation of a lower λ-leveling kernel within the Geostoch software library (Mayer et al. 2004). The algorithm has been suggested by Couprie et al. (2001). Considering a digital greyscale image on a set $I \subset \mathbb{Z}^2$ of pixels as a map $g : I \longrightarrow \{0, \ldots, 255\}$, the goal of the algorithm is to extract the crest-lines of the image topology as defined by the greyscales (Fig. 2 (b)). However, in order to avoid an oversegmentation of noisy images, crest lines of insufficient contrast are neglected. The algorithm follows an iterative philosophy, which modifies the greyscale topology in a controlled way by lowering greyvalues of single pixels according to a set of rules regarding the 8-neighborhood of the pixel. Crest-lines arising throughout this procedure are not subject to further modification unless their contrast (i.e. the smallest greyvalue difference to a neighborhood pixel) does not exceed the parameter λ. For details we refer to Couprie et al. (2001). A key feature of the algorithm is that within the 8-neighborhoods, greyvalue differences are considered rather than the actual greyscale. Therefore, the crest lines resulting from filament trajectories of low greyscales in the background of the image will still be identified by the algorithm as long as their contrast to the background is sufficient. For our image data, lower λ- leveling kernels were computed for $\lambda = 10$ after noise in the original SEM images had been reduced by means of the anisotropic diffusion filter in ImageJ (Rasband 1997-2010). A lower λ-leveling kernel is closely related to a watershed transform with local minima of neighborhood contrast greater than λ as markers. Nevertheless, in contrast to the watershed transform not all of these minima will define an own mesh within the network of crest lines, since neighborhood contrast can change due to the iterative nature of the algorithm. Although this feature reduces the risk of oversegmentation, a certain degree of oversegmentation could not be avoided unless the filter parameter λ was set to values which also suppressed the identification of the darker background filaments (Fig. 2 (c)). Oversegmentation occurred especially within the bright filaments of the foreground, where the variability of greyvalues was still rather high.

2.2 Reducing oversegmentation

In order to reduce the oversegmentation within the lower λ-leveling kernels of the SEM data, the binarized crest lines (Fig. 2 (c)) were in a first step dilated by 2 pixels (this corresponds to approximately half the filament diameter), i.e. all pixels whose distance to a crest line did not exceed two pixels were classified as foreground and colored white. The resulting image was then added to a binarized version of the original SEM image, where the latter was computed by means of a standard intermode threshold (Fig. 2 (d)). All of these steps were performed using the ImageJ software yielding a binarization of the original SEM images with the following desirable properties. First of all,

the dark background filaments, which were not identified by the intermode thresholding, were incorporated into the binarization through their dilated crest lines. Moreover, the majority of pseudo-meshes resulting from oversegmentation were either closed by the dilation or by the subsequent superposition of the dilated crest lines with the threshold image. Finally, an important aspect of this binarization strategy is the suppression of background noise, which would have been part of a simple binarization by a threshold low enough to incorporate dark background filaments.
In a final step the standard skeletonization algorithm of ImageJ was applied to the binarized images. This way the network structures were thinned to fibers of one pixel width (Fig. 2 (e)). It is noticeable that in Fig. 2 (e) the majority of the oversegmentation artifacts in Fig. 2 (c) has been removed, though most dark background filaments are still represented in the segmentation. The drawback of the binarization technique is that closely parallel filament strands may get merged in the dilation step and will consequently be represented by a single fiber in the final skeleton.

2.3 Detection of pseudo cross-links

Our analysis is based on 2D images of a possibly multi-layered 3D network structure. The 2D perspective of the microscope and the resulting skeleton of the network graph (Fig. 2 (e)) frequently suggest the existence of cross-links, where filament trajectories do not have an actual contact in 3D (see the red arrows in Fig. 2 (a)). However, the correct definition of cross-links and thus network connectivity is crucial for the computation of morphologically relevant parameters such as mean edge length and network meshes (see Sections 3.1, 3.2, and 3.3). Therefore we implemented a classification algorithm removing pseudo cross-links from the network graph. In a first step a Canny-Deriche edge detection filter (Canny 1986, Deriche 1987) was applied to the original SEM images in order to compute a gradient image detecting the filament boundaries. Due to specific properties of the secondary electron signal, greyvalue gradients along filament boundaries in the top of the specimen were particularly high and could thus be extracted from the gradient images by simple thresholding. Whenever pseudo cross-links occur in the skeleton, the trajectory of a lower level filament in the skeleton crosses the high edge gradient of an upper-level filament in the vicinity of the pseudo-node (Fig. 2 (f)). Filament trajectories intersecting the gradients were therefore split into two parts and the shorter of the two resulting pixel paths was removed from the skeleton. This way pseudo cross-links in the upper network layer could be removed and thus, edges and meshes could be correctly identified for the top layer of the network. Filament trajectories in the extracted skeletons were not always optimally centered within the filaments and sometimes even touched the boundary of the filament they were tracking. In order to preserve such filament trajectories during cross-link classification, the algorithm was not applied to the original thresholded gradient images but gradient particles of less than

10 pixels size were removed and afterwards the distance of pixelpaths representing opposite boundaries of a filament was slightly enlarged. This was done by means of the method BinaryDilateNoMerge8, which is part of the collection of morphological operators for ImageJ provided by Landini (2010). The algorithm perfoms a dilation of a binary image without merging particles together and thus leaves a gap between the dilations of opposite filament boundaries. Subsequent skeletonization of the dilated image yields the desired version of the gradient image with increased distance of opposite filament boundaries.

2.4 Vector data

The pixelpaths representing the filament trajectories were finally converted into vector data. Since filaments exhibited only negligible curvature, trajectories were represented by line segments. Some filaments were entangled in such a way that they enclosed small angles, which leads to the artifacts of cross-links located very closely to each other and network edges shorter than filament diameters. Therefore, as suggested in Beil et al. (2005) and Lück et al. (2010), such pairs of cross-links were merged into a single one located in their center of gravity. Taking into account that after carbon coating filaments had a diameter between 20 and $25nm$, merging was performed for cross-links of a distance no more than $25nm$ apart in ascending sequence, i.e., cross-links of smaller distance were merged first. Cross-links were defined as vertices of the network graph with degree of at least 3, where the degree counts the number of edges emanating from a vertex. Thus, positions of dead ends in the network graph as arising through cross-link classification were not modified by the merging algorithm.

3 Statistical analysis of network morphology

Based on the network graphs extracted from the SEM image data a statistical analysis of network morphology was conducted, aiming at the comparison of network structure between different cell types of mesenchymal lineage, namely MSCs, OBs and the differentiated and dedifferentiated state of chondrocytes CH1 and CH2. Samples were analyzed separately for the cell periphery and the perinuclear cellular compartment. A total of 138 images was statistically analyzed, where sample sizes varied between 15 and 20 images per cell type and cellular compartment. Images were taken from 5 (MSC, OB) and 6 (CH1, CH2) different cells, respectively. Each image covered an area of $7.2\mu m^2$.

3.1 Mean value characteristics of network morphology

In this section we compare mean value characteristics of the network morphology found for the cell types described above. For each image we computed the

mean network length per unit area and the mean edgelength. In our 2D image data edges could only be investigated by measuring their 2D projections. However, these approximations can be expected to be rather accurate since most filaments were oriented parallel to the imaging plane. Edgelengths were computed for all edges whose center was located in a subwindow of the image in order reduce edge effects of the estimation. For construction of the subwindow, the image was reduced by $0.25\mu m$ at each side. Spatial mean values of the edgelength were computed with respect to all edges in the top layer of the network, i.e. for all egdes that were not truncated during classification of cross-links (see Section 2.3).

Results are visualized by boxplots in Tab. 1. It is noticeable that there is a substantial morphological variability of network architecture between different images taken for a single cell type and compartment. Differences between sample means were tested for significance using the Tukey-Kramer multiple comparisons procedure (TKT) (Kramer 1956) if the Shapiro Wilk test did not indicate violations of the normality assumption. The additional assumption of equal sample variances for the TKT was for none of the characteristics rejected by the Brown-Forsythe test at a 5% level of significance (R-software package). For characteristics where the normality assumption was violated we used pairwise Wilcoxon rank tests with (a very conservative) Bonferroni correction, even if this may have reduced the power of testing in comparison to the TKT. Tabelled p-values for the TKT and the WRT have thus been adjusted for multiple testing. Note that all test results are therefore conservative (see e.g. Hayter (1984)).

Morphological differences between the different cell lines were rather small in the perinuclear compartments, whereas they were pronounced in the cell periphery. In the peripheral compartment MSCs exhibited the highest total network length per unit area, followed by the OBs, whereas early and late chondrocytes (CH1 and CH2) showed rather sparse IF networks (Tab. 1). This observation corresponded to small mean edge lengths in the MSCs, which were slightly larger for the OBs and substantially increased in the CH1 and CH2 cells (Tab. 1). For the cell periphery, with respect to both network characteristics, mean network length per unit area as well as mean edge length, the TKT identified two groups of significantly different classes of cell types at the 5%-level. The first group is formed by the early stage chondrocytes CH1, the second one by MSC and OB cells (Tab. 2 and 3). Differences within the two groups were not significant. Comparisons of late stage chondrocytes (CH2) to MSCs and OBs generally showed similar results as obtained for the earlier harvested CH1 cells. However, the mean edge length of CH2 cells was not found to significantly differ from OBs by the TKT ($p = 0.1$). A pairwise comparison by a WRT without Bonferroni correction however indicated significant differences ($p = 0.01$).

For the perinuclear compartment differences of the mean value characteristics were not statistically significant at the 5%-level according to the ANOVA F-test and pairwise TKTs (Tabs. 2 and 3).

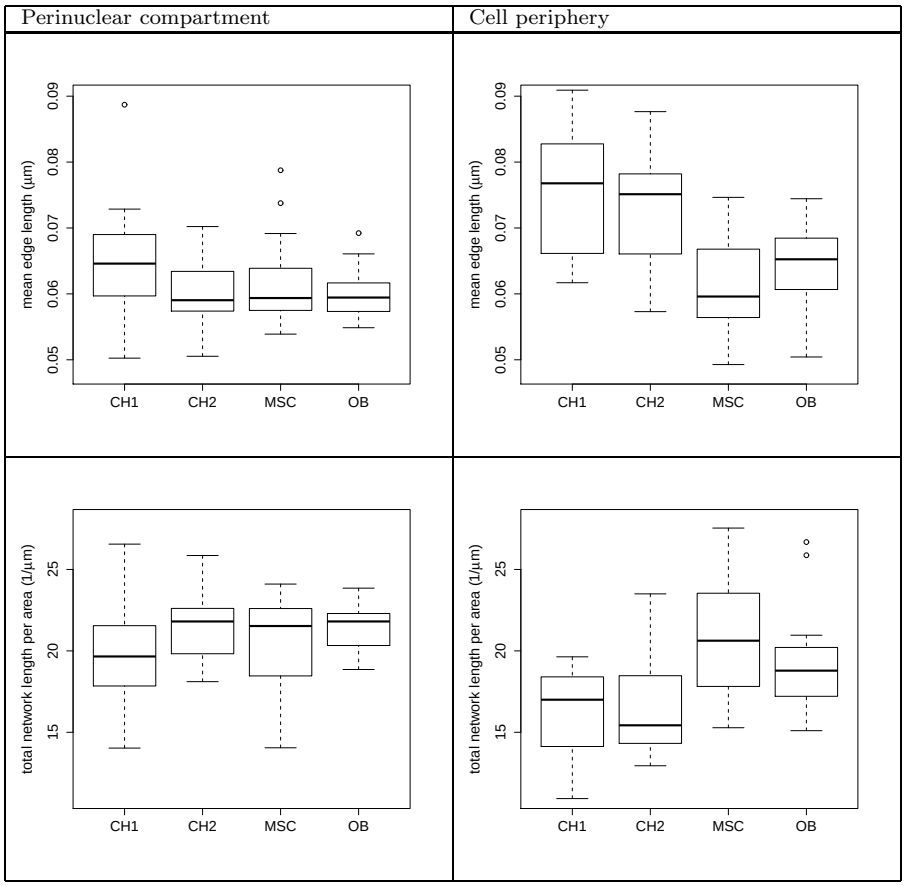

Table 1 Morphological mean value characteristics of the network in the **perinuclear compartment** and the **cell periphery**. Spatial mean values were computed for single images representing a biological scenario. The boxplots visualize the samples of these mean values derived from multiple images.

	Periphery			Perinuclear compartment		
	CH2	MSC	OB	CH2	MSC	OB
CH1	0.67	$< 10^{-4}$	$< 10^{-2}$	0.17	0.56	0.15
CH2		$< 10^{-3}$	0.037		0.87	0.99
MSC			0.66			0.85

Table 2 Adjusted p-values of the Tukey-Kramer multiple comparison test for the equality of **mean edge lengths**.

	Periphery			Perinuclear compartment		
	CH2	MSC	OB	CH2	MSC	OB
CH1	0.98	$< 10^{-3}$	0.047	0.26	0.93	0.29
CH2		$< 10^{-3}$	0.1		0.6	0.99
MSC			0.4			0.62

Table 3 Adjusted p-values of the Tukey-Kramer multiple comparison test for equality of **mean network length per unit area**.

3.2 Network elasticity

We will now illustrate that the morphological differences found above can have a substantial impact on the mechanical properties of a vimentin IF network. For this purpose we follow Lin et al. (2010) and apply a formula estimating the elastic plateau shear modulus G of a vimentin network in the elastic regime that has been derived by MacKintosh et al. (1995). For a uniform or affine strain, the elastic network shear modulus is given by

$$G = 6\rho\frac{k_b T \ell_p^2}{\ell_e^3}, \tag{1}$$

where k_b is the Boltzmann constant, T denotes temperature, ℓ_e is the mean edge length, and ρ denotes the mean network length per volume, also referred to as network density. The constant ℓ_p is the persistence length of the filaments, which is the maximum distance over which two points on a single filament move in a correlated way while the filament gyrates under thermal fluctuations. For vimentin not adsorbed to a surface, a value of $\ell_p = 0.5\mu m$ has been estimated (Mücke et al. 2004, Schopferer et al. 2009). T was chosen as body temperature. Notice that for our 2D image data ℓ_e and ρ can only be estimated from planar projections of the network. Since electron-tomographic 3D data of IF networks of similar network density revealed that 2D SEM images visualize the networks within a depth of $\sim 0.5\mu m$ (Lück et al. 2010) this value was used for estimating ρ from our measurements of total network length. Formula (1) has been derived for isotropic 3D networks. Although most of the IFs in our image data are oriented rather parallel to the imaging plane, the formula can nevertheless give an approximation of the mechanic effects of morphological network variability (Fleischer et al. 2007).

The boxplots in Fig. 3 visualize the computed shear moduli for the IF networks in different cell types and cellular compartments. Differences between cell types with respect to network elasticity were small for the perinuclear compartments and not significant according to the ANOVA F-test and pairwise TKT (Tab. 4), whereas they were pronounced in the cell periphery. In the periphery MSCs and OBs with their very dense IF networks exhibited significantly higher shear moduli than the chondrocytes (Tab. 4, where we used a Bonferroni-corrected WRT due to non-normally distributed samples). An exception were the non-significant deviations between CH2 and OB cells ($p = 0.07$), which were however classified as significant by a pairwise WRT ($p = 0.012$). In the cell periphery elasticity differences between the two stages

of chondrocytes CH1 and CH2 ($p = 0.1$) as well as between OBs and MSCs ($p = 0.87$) were not significant according to the Bonferroni corrected WRT . In addition to the elastic shear modulus G we investigated the characteristic stress σ_c at which the vimentin network leaves the linear elastic regime and responds to further increases of shear stress with nonlinear stiffening. According to Lin et al. (2010) σ_c is given by

$$\sigma_c = \rho \frac{k_b T \ell_p}{\ell_e^2}. \tag{2}$$

In the cell periphery this stress stiffening onset was significantly higher for the OBs and the MSCs if compared to CH1 and CH2 cells (Tab. 5). As an exception, the difference between CH2 and OB cells was not significant ($p = 0.07$) according to the Bonferroni corrected WRT though by a pairwise WRT ($p = 0.012$). The highest values of σ_c occurred for single very dense network samples from MSCs (Fig. 4 and Tab. 5). In the perinuclear compartment the ANOVA F-test and the TKT did not detect any significant differences between mean stress stiffening onsets of the different cell types at the 5% level (Tab. 5). In vitro experiments of Lin et al. (2010) showed that at a fixed network density ρ vimentin networks can be stiffened by the addition of cations which crosslink vimentin tail domains, thus reducing the mean edge length ℓ_e. In order to investigate whether such structural modifications of network architecture at a fixed network density also occur in cellular systems, we studied the relation between ρ and ℓ_e for our image data. Generally, ρ scales with $1/\ell_e$ (Fig. 5 (a)). Nevertheless, as will be demonstrated below, the measured regression residuals are large enough to substantially alter cellular elasticity. Fig. 5 (b) illustrates the effect of the variations in mean edge length found for our image data on the elastic network shear modulus G. Based on the regression results, a network density-dependent mean modulus $G(\rho)$ was computed (black line in Fig. 5(b)). This was achieved by substituting the value $\widehat{\ell_e^{-1}}(\rho)$ as predicted by the regression line for ℓ_e^{-1} in formula (1). In an analogous way upper and lower envelope curves $G_u(\rho)$ and $G_l(\rho)$ were obtained. For this purpose ℓ_e^{-1} was replaced by $\widehat{\ell_e^{-1}}(\rho) + r$, $r \in \{r_u, r_l\}$, where r_u and r_l denote the 95%-quantile of the positive and negative regression residuals, respectively. This way the effects of the additional variability of mean edge length as found in the data were introduced into the elasticity model (red and blue lines in Fig. 5(b)). The envelope curves indicate that for lower values of ρ, cells are able to vary the elastic shear modulus of their IF network by a factor 2 through a mere modification of mean edge length, while the total amount of filamentous vimentin is kept constant.

3.3 Second order characteristics of network morphology

In view of the relation between different network mean-value characteristics discussed above the question arises, whether there is also a local variability of network structure which can affect network mechanics. We investigated such

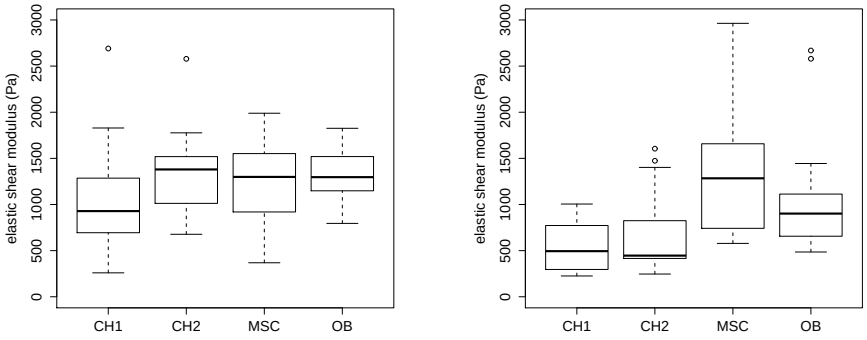

(a) (b)

Fig. 3 Elastic shear modulus of the network in the **perinuclear compartment** (a) and in the **cell periphery** (b). Values were computed for each of the single images representing a biological scenario. The boxplots visualize samples with respect to a biological scenario, which were derived from multiple images.

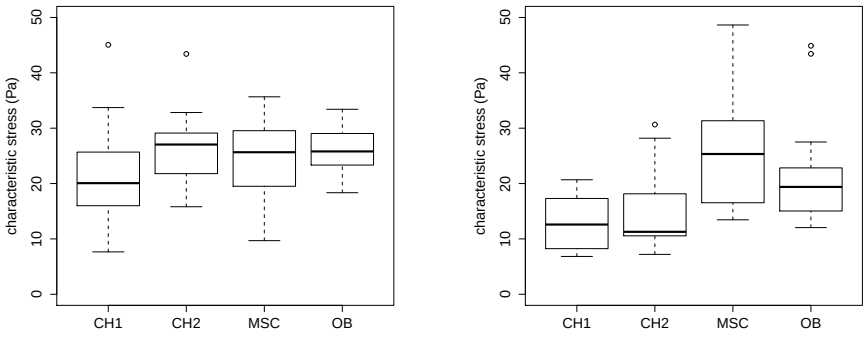

(a) (b)

Fig. 4 Characteristic onset of stress stiffening of the network in the **perinuclear compartment** (a) and in the **cell periphery** (b). Values were computed for each of the single images representing a biological scenario. The boxplots visualize samples with respect to a biological scenario, which were derived from multiple images.

	Periphery			Perinuclear compartment		
	CH2	MSC	OB	CH2	MSC	OB
CH1	1	$< 10^{-3}$	0.024	0.41	0.84	0.47
CH2		$< 10^{-2}$	0.07		0.88	0.99
MSC			0.87			0.9

Table 4 Adjusted p-values of the Tukey-Kramer multiple comparison test (perinuclear) and the Bonferroni-corrected Wilcoxon rank test (periphery) for the equality of **shear moduli**.

	Periphery			Perinuclear compartment		
	CH2	MSC	OB	CH2	MSC	OB
CH1	1	$< 10^{-3}$	0.025	0.34	0.83	0.38
CH2		$< 10^{-3}$	0.071		0.84	0.99
MSC			0.81			0.85

Table 5 Adjusted p-values of the Tukey-Kramer multiple comparison test (perinuclear) and the Bonferroni corrected Wilcoxon rank test (periphery) for the equality of **stress stiffening onsets**.

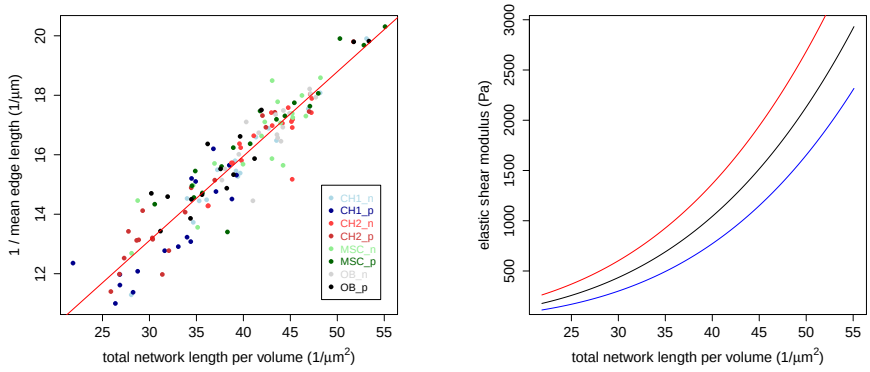

(a) (b)

Fig. 5 (a) Network density plotted against the mean edge length. The suffixes 'n' and 'p' refer to the perinuclear compartment and the cell periphery, respectively. Network density ρ generally scales with the reciprocal of mean edge length $1/\ell_e$. However, at fixed ρ differences in mean edge length can still substantially modify the elastic modulus G of the network. In (b) G is plotted as a pure function of network density (black line), where the parameter $1/\ell_e$ in formula 1 has been replaced with the predicted value according to the regression line in (a). The red and blue lines show the values obtained for G, when the 95% quantile of the positive and negative regression residuals is added to the predicted regression value of $1/\ell_e$, respectively.

second order characteristics of network morphology by means of the pair-correlation function $g : [0, \infty) \longrightarrow [0, \infty)$ of the point pattern of mesh centers in the upper network layer. Before we will discuss estimation results and relate them to cell mechanics we will give a formal definition of $\widehat{g}$. Let $\{X_n\}_{n\geq 1}$ be a sequence of $\mathbb{R}^2$-valued random vectors defining a point process in $\mathbb{R}^2$, which has almost surely only finitely many points in each bounded Borel set B such that none of the points coincide with probability 1. Then $\{X_n\}_{n\geq 1}$ is called stationary if

$$\{X_n\}_{n\geq 1} \stackrel{d}{=} \{X_n + x\}_{n\geq 1} \text{ for all } x \in \mathbb{R}^2,$$

where the equality in distribution refers to the entire point process (for a formal definition see e.g. Daley and Vere-Jones (2003/08)). Moreover, $\{X_n\}_{n\geq 1}$ is called isotropic if

$$\{X_n\}_{n\geq 1} \stackrel{d}{=} \{\delta(X_n)\}_{n\geq 1} \text{ for all rotations } \delta \text{ around the orign.}$$

The intensity measure μ of $\{X_n\}_{n\geq 1}$ is defined as

$$\mu(B) = \mathbb{E}\sum_{n\geq 1} \mathbb{1}_B(X_n) \text{ for all } B \in \mathcal{B}(\mathbb{R}^2),$$

where $\mathcal{B}(\mathbb{R}^2)$ denotes the Borel $\sigma-$algebra. Thus, $\mu(B)$ is the expected number of points in the set B. If $\{X_n\}_{n\geq 1}$ is stationary one has $\mu = \lambda\nu$, where ν denotes 2-dimensional Lebesgue measure and the constant $\lambda > 0$ is called the intensity of $\{X_n\}_{n\geq 1}$. Analogously one defines the second factorial moment measure by

$$\alpha^{(2)}(B_1 \times B_2) = \mathbb{E}\sum\nolimits^{\neq}_{n,m\geq 1} \mathbb{1}_{B_1}(X_n)\mathbb{1}_{B_2}(X_m) \text{ for all } B_1, B_2 \in \mathcal{B}(\mathbb{R}^2),$$

which describes the expected number of point pairs (X_n, X_m) with values in $B_1 \times B_2$, where $n \neq m$. We now consider the case that $\alpha^{(2)}$ is absolutely continuous with respect to the 4-dimensional Lebesgue measure and thus there exists a density $\rho_2 : \mathbb{R}^4 \longrightarrow [0, \infty)$ such that

$$\alpha^{(2)}(B_1 \times B_2) = \int_{B_1}\int_{B_2} \rho_2(x_1, x_2)dx_2dx_1 \text{ for all } B_1, B_2 \in \mathcal{B}(\mathbb{R}^2).$$

In case $\{X_n\}_{n\geq 1}$ is stationary and isotropic the value $\rho_2(x_1, x_2) = \rho_2(r)$ depends only on the distance $r = |x_1 - x_2|$. The *pair-correlation function* $g : [0, \infty) \longrightarrow [0, \infty)$ is defined as

$$g(r) = \frac{\rho_2(r)}{\lambda^2} \text{ for all } r \geq 0.$$

For a homogeneous Poisson process with intensity λ, which can be seen as a reference model for complete spatial randomness, one can easily show that $\alpha^{(2)}(B_1 \times B_2) = \lambda^2\nu(B_1)\nu(B_2)$ and hence $g(r) = 1$ for all $r \geq 0$. Therefore, the pair-correlation function of a point pattern can be interpreted as follows. For $r > 0$ such that $g(r) > 1$ there are more point pairs with distance r than in a Poisson process of the same intensity λ. Vice versa, in case $g(r) < 0$ there are less point pairs with distance r than in a Poisson point process. An estimator $\widehat{g}(r)$ for the pair-correlation function of a point process $\{X_n\}_{n\geq 1}$ on some bounded observation window $W \subset \mathbb{R}^2$ is given by

$$\widehat{g}(r) = \frac{1}{\widehat{\lambda}^2(W)} \sum\nolimits^{\neq}_{n,m\geq 1} \frac{K\big((|X_n - X_m| - r)/b\big)\mathbb{1}_{W\times W}(X_n, X_m)}{2b^2\pi r\nu(W \cap (W + (X_n - X_m)))}, \tag{3}$$

where $\widehat{\lambda}(W) = \dfrac{1}{\nu(W)} \displaystyle\sum_{n\geq 1} \mathbb{1}_W(X_n)$ denotes the standard estimator for λ, and K is some kernel function.

For our estimation results discussed below, K was chosen as the Epanechnikov kernel with bandwidth $b = 0.15/\sqrt{\widehat{\lambda}}$ as recommended in Stoyan and Stoyan (1994). If the estimator (3) is computed for an anisotropic point pattern, it

contains aggregated information of inter-point distances with respect to different directions.

Fig. 6 shows pair-correlation functions for the point pattern of mesh centers in the top network layer of our image data, where these points were defined as the centers of maximum incircles to be inscribed into top layer meshes. The pair-correlation functions $\widehat{g}(r)$ in Fig. 6 are argument-wise averages with respect to the estimation results obtained for the single images of a biological scenario. The averaged estimated functions $\widehat{g}(r)$ were of similar shape for all cell types and compartments considered. Due to the merging of closely located cross-links during image segmentation pairs of mesh centers with distance less than $25nm$ hardly occurred, although they are theoretically not excluded by the merging algorithm. Consequently, the estimations of $\widehat{g}(r)$ showed values close to 0 for $r < 25nm$. All pair-correlation functions exhibited a peak around $50nm$, which implies that point-pair distances in this range are more frequent than in a Poisson process with the same intensity and thus indicates a clustering effect of the points. The mean degree of clustering, as indicated by the height of the peaks, showed slight variations between different cell types. However, the variation of the estimated pair-correlation functions computed for single images of a cell type and compartment was substantially larger than the differences of the mean values displayed in Fig. 6. In order to visualize the variability of the clustering effects within single scenarios, we defined a clustering parameter

$$\gamma = \int_{[a,b]} \widehat{g}(r)dr,$$

where $[a, b] = [25nm, 100nm]$, and thus $\widehat{g}$ is integrated in the range identified as relevant for clustering (Fig. 7). With respect to γ tests did not detect significant differences between biological scenarios. This suggests that mesh cluster formation is mainly a source of morphological variability within single biological scenarios.

In order to investigate whether mesh clustering can be related to the regulation of network mechanics the clustering parameter γ was introduced as a second explanatory variable into the regression model relating the network density ρ to the reciprocal ℓ_e^{-1} of the mean edge length. t-Tests for significance of single explanatory model parameters classified the effects of both variables ρ and γ as highly significant ($p < 10^{-5}$). Backward elimination of explanatory variables yielded highly significant loss in goodness of fit when γ was excluded from the model ($p < 10^{-5}$). The regression plane fitted to the data can be seen in Fig. 9 and indicates that a linear combination of network density ρ and the clustering parameter γ explains the mean edge length rather well. The decreasing effect of mesh clustering on the mean edgelength can also be demonstrated on a model-based level. For this purpose we compared two scenarios of a stochastic simulation model for the formation of single layered IF networks published by Beil et al. (2009), which were identified to result in weak and strong clustering of network meshes (Fig. 8). For the simulations network density was kept constant at $\rho = 49\mu m^{-2}$. Comparison of two samples, each

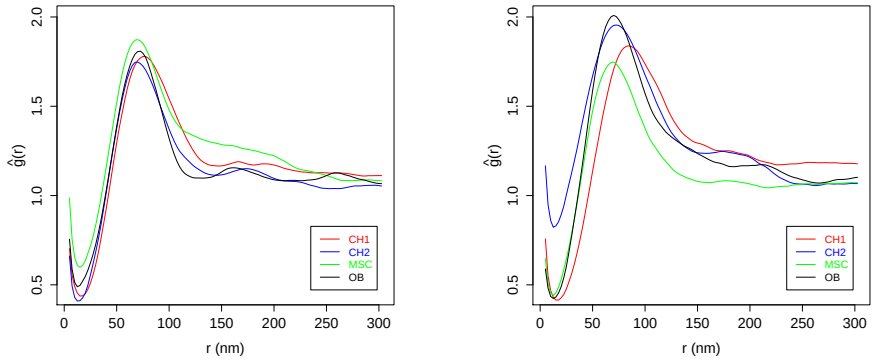

(a) (b)

Fig. 6 Pair-correlation functions of upper-layer mesh centers in the **perinuclear compartment** (a) and the **cell periphery** (b). The estimated values $\widehat{g}(r)$ are argument-wise averages over the corresponding estimates obtained for single images.

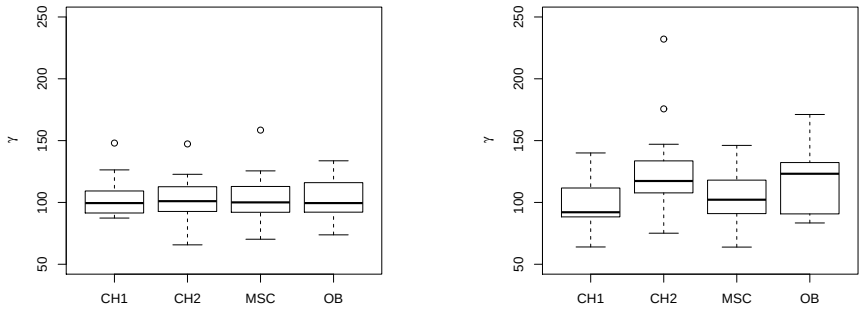

(a) (b)

Fig. 7 Integrals γ of the **Pair-correlation functions** of mesh centers in the **perinuclear compartment** (a) and the **cell periphery** (b) for single images.

consisting of 100 realizations, showed a decrease of mean edge length by 12% in the strongly clustered networks in comparison to the weakly clustered scenario. By formula (1) this corresponds to an increase of the elastic modulus by a factor 1.5 at a network density of $\rho = 49\mu m^{-2}$. The factor 1.5 closely resembles the spread between the envelope curves in Fig. 5(b) at $\rho = 49\mu m^{-2}$, which estimate elasticity differences between weakly and strongly clustered network morphologies in our real network data.

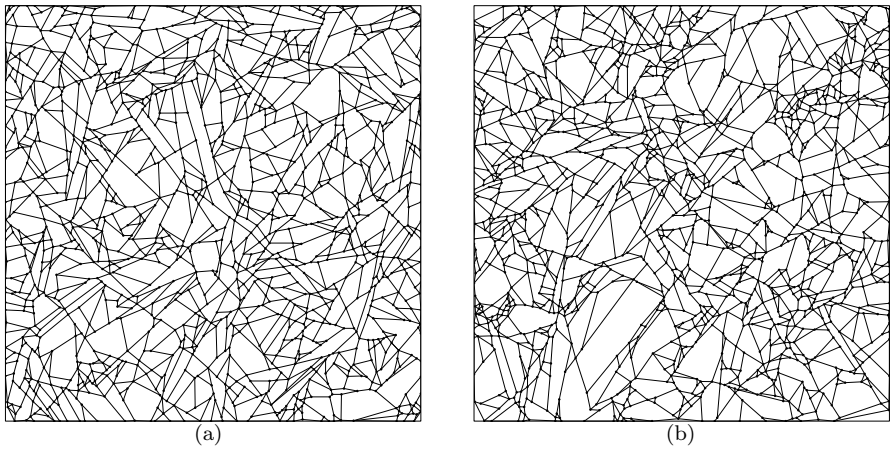

Fig. 8 Simulated single-layered network morphologies with weak (a) and stronger (b) clustering of network meshes at constant mean network density. Mesh clustering resulted in a 12% decrease of mean edge length and an increase of the elastic shear modulus G by a factor 1.5.

4 Discussion

The cytoskeleton is known to play a vital role in the process of mesenchymal differentiation. So far studies have primarily investigated changes of the actin network (Darling et al. 2008, Docheva 2008, Rodríguez et al. 2004, Yourek et al. 2007). The spatial and structural organization of the actin network has even been proposed as a biomarker for early prediction of stem cell lineage fates during the differentiation process (Treiser et al. 2010). From the morphologoical point of view the focus of previous research has been on gross levels of protein expression, global intracellular protein distribution and the observation of thick stress fibers as resolved by light microscopy. Additionally, extensive measurements of cellular elasticity have been conducted by various mechanical testing methods (an overview is given in Darling et al. 2008). So far there has been rather limited attention to the role of IFs during mesenchymal differentiation. The IF protein vimentin, which is dominantly expressed in cells of mesenchymal lineage, has been reported to participate in chondrogenic differentiation (Bobick et al. 2010). This motivated our analysis of differences in network ultrastructure arising during the differention process of mesenchymal stem cells into osteoblasts and chondrocytes. We have demonstrated that in chondrogenic direction there is a substantial decrease in network density and a corresponding increase of the mean edge length in the cell periphery, whereas OBs exhibit an IF network which is not severely different from MSCs. Few of the MSCs nevertheless showed a particularly high network density in their periphery, which could not be found for the other cell types. We did not find significant alterations in network morphology in the perinuclear compartments. Our observation of pronounced network reorganization in the cell

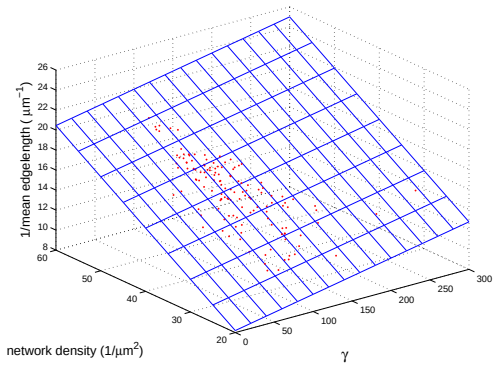

(a)

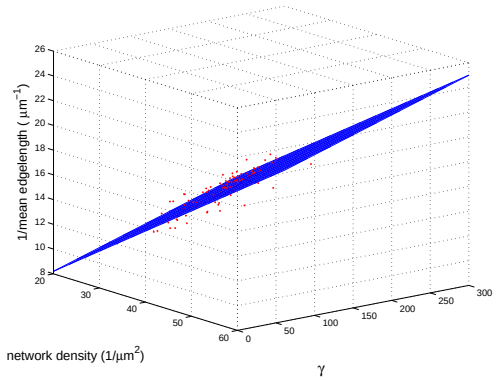

(b)

Fig. 9 Linear model relating the reciprocal of mean edgelength $1/\ell_e$ to network density ρ and clustering parameter γ.

periphery corresponds to fluorescence imaging experiments by Windoffer et al. (2004), which identified the cell periphery as a center for network remodeling of keratin IF networks.

Atomic force microscopy (AFM) showed that osteoblasts are substantially stiffer than chondrocytes (Darling et al. 2008). Since AFM primarily resolves the actin network (Yourek et al. 2007) these findings cannot be directly linked to the morphological differences of the IF network in OBs and CHs but should rather be interpreted as a consequence of a differing actin network architecture. However, our results suggest that the reorganization of the actin network during chondrogenesis is accompanied by a remodeling of the IF network, which is crucial for the cellular response to large deformations that cause a disruption of the stiffer actin cytoskeleton. Darling et al. (2008) and Yourek et al. (2007) report the Young's modulus of OBs to be higher than that of MSCs. Our data suggests that this effect is not reflected by significant morphological differences in the IF network, which is rather dense in both cell types. Since MSCs and OBs show a rather high migratory activity (Fiedler et al. 2005, Fiedler et al.

2006, Nakasaki et al. 2008), the high network density of their IF cytoskeleton may meet a demand for an increased robustness with respect to large scale deformations during migration. On the other hand chondrocytes exhibit less migration activity (unpublished observations). This is reflected by a reduction of their IF network density in the periphery as demonstrated in our work. Our data indicates that the IF network is a highly dynamical system exhibiting substantial local variations of its morphology even within single cells. By modifications of network structure cells can adapt their mechanical properties to the various needs arising during migration as well as mitosis.

Our data was obtained from detergent extracted and critical point dried samples, which were imaged by SEM. These techniques yield a high level of contrast, which is necessary for automatic image segmentation and hence allows for the analysis of large samples of images. Possible preparation artifacts for these protocols such as surface tension artifacts caused by traces of water during critical point drying (Ris 1985) and fracturing of actin filaments (Resch et al. 2002, Urban et al. 2010, Vignal and Resch 2003) have been discussed in the literature. Comparisons of critical point dried samples with freeze dried controls by Sailer et al. 2010 did not show obvious morphological differences for keratin IF networks. Moreover, in the latter study detergent extracted and critical point dried samples were also compared with ultrathin sections of unextracted high-pressure frozen and freeze-substituted cells, thus using - as generally considered- the best immobilization method for the preservation of subcellular structures (e.g. Dubochet 2007, Hohenberg et al. 2003). Since these comparisons did not indicate differences in network structure between the preparation techniques, we are in particular confident that network tension in our samples was not altered by preparation. This view is additionally supported by the preservation of outer cell shape which indicates unchanged boundary conditions. In Sailer et al. 2010 specimens, which had been detergent extracted by the protocol used in our study, were compared to samples where prior to detergent extraction the actin network had been stabilized by treatment with phalloidin. After freeze drying and tungsten coating IFs could be distinguished from actin by the helical surface structure of actin filaments. The results indicate that without phalloidin treatment the extraction protocol reliably removes the actin component of the cytoskeleton. We can therefore assume that our samples only contained the IF component of the cytoskeleton.

Our quantitative measurements of network characteristics were obtained by a fully automatic image segmentation algorithm, which allows for a high-throughput analysis of cytoskeleton images without bias introduced by manual segmentation. For the first time an image segmentation method was used, which is suitable for the analysis of 2D images of multilayered IF networks with large differences in the greyscale of IFs in different layers. Greyvalue differences between filament trajectories intersecting each other in the 2D images without contact in 3D were used to eliminate cross-link artifacts in the 2D network graphs. Classification of cross-links has substantially contributed to the understanding of actin networks (Urban et al. 2010) and represents a

crucial step for the interpretation of cytoskeleton image data. Our algorithm provides an automatic approach to this segmentation step, which is suitable for high-throughput studies of network morphology.
Despite our greyvalue-oriented segmentation approach some filaments in lower network layers were not detected by the algorithm. Consequently, our measurements of total network length are still slight underestimates taking additionally into account that filament orientations were assumed parallel to the imaging plane. Due to the latter assumption our measurements of mean edge lengths are also slight underestimates. Moreover, the shorter an edge in a lower network layer the more likely is its complete visibility in a 2D image. Consequently, the likelihood of a lower level network edge to be considered for the computation of the edge length distribution decreased with length. However, the vast majority of completely visible edges would have been visually classified as part of the top network layer.

By means of mean-value formulae for the elastic modulus and the characteristic stress for the onset of stress-stiffening we demonstrated that the changes in IF network morphology between chondroctytes on the one side and osteoblasts and mesenchymal stem cells on the other have a dramatic impact on elastic properties of the IF network and hence on cellular functionality. Whereas it cannot be expected that these mean-value approaches capture the complex interplay of mechanical properties and network morphology in semiflexible polymer networks to full extend, finite element simulations suggest that they take into account the morphological factors with most dominant impact on network mechanics (Huisman et al. 2007), namely network density and mean edge length. Due to the 2D nature of our data, we could only estimate the observed 3D volume and thus the network density ρ from tomographic data of IF networks published in Lück et al. (2010), which were imaged with the same microscopy and preparation method and exhibited a similar network density. Results for the elastic shear moduli estimated for our cell types were however qualitatively identical, when formulae (1) and (2) were reformulated in terms of the mean meshwidth ξ, which according to Morse (1998) is roughly of the order $1/\sqrt{\rho}$ and can be assessed by the diameter of a maximum incircle to be inscribed into top-layer meshes (Fleischer et al. 2007). The question arises whether all investigated network samples were within a linear elastic stress-strain regime. However, in view of the large strains between 30 and 40% required for the onset of stiffening in solutions of vimentin filaments and hagfish slime threads composed of IF proteins (Janmey et al. 1991, Fudge et al. 2003) a non-linear stress response can only be expected for networks subject to large deformations. For cells adherent to flat surfaces such as our saphhire discs large deformations of the cell as a whole are not likely to occur without external mechanical impact, since even migration would not require strong variations in cell shape as e.g. occurring when cells squeeze through small pores. Strong locally confined deformations resulting from an interplay between migration and adhesion can however not be completely excluded for our cells. We nevertheless expect the vast majority of the IFs in our samples to be in the linear stress-strain regime.

One of our most interesting findings is that although the reciprocal $1/\ell_e$ of the mean edge length scales roughly linearly with network density ρ, we observe considerable variability of measured mean edge lengths around the value predicted by the regression line. These structural differences in network architecture rather than in the total amount of filamentous vimentin can account for elasticity differences of a factor 2 at moderate values of ρ. This indicates that cells use an energy-efficient and presumably also fast mechanism for the structural modification of their IF network beyond variations in the concentration of filamentous vimentin in order to tune their mechanical properties. This seems to be a universal principle, which can also be observed in IF networks composed of other proteins such as keratin (Beil et al. 2009, Lück et al. 2010). By means of a stochastic simulation model for the generation of IF network morphologies we demonstrated that at constant network density ρ variations of the mean edge length can be mediated by the formation of mesh clusters. Since in our microscopy data the clustering parameter γ had a high explanatory power in the linear regression model relating $1/\ell_e$ to ρ and γ , variations of mesh clustering are apparently a crucial factor controlling ℓ_e in real cells. Biochemically, network structure can be regulated by the concentration of the divalent cations Ca^{2+} or Mg^{2+}, which is also known to mediate guided motility of osteoblast-like cells (Ozkucur et al. 2009). *In vitro* studies by Lin et al. (2010) showed that Ca^{2+} or Mg^{2+} cations modify the carboxyterminal vimentin tail domains and this way control cross-link formation, which in turn determines the edge length distribution and hence network stiffness. Our statistical image analysis of SEM data suggests that such mechanisms may also be used for network remodeling in living cells of mesenchymal lineage. Through their impact on locally defined aspects of network morphology such as mesh clustering they can substantially alter mechanical cellular properties.

References

1. Beil M, Micoulet A, von Wichert G, Paschke S, Walther P, Omary MB, Van Veldhoven PP, Gern U, Wolff-Hieber E, Eggermann J, Waltenberger J, Adler G, Spatz J, Seufferlein T (2003) Sphingosylphosphorylcholine regulates keratin network architecture and viscoelastic properties of human cancer cells. Nat Cell Biol 5:803-811
2. Beil M, Braxmeier H, Fleischer F, Schmidt V, Walther P (2005) Quantitative analysis of keratin filament networks in scanning electron microsopy images of cancer cells. J Microsc 220: 84–95
3. Beil M, Lück S, Fleischer F, Portet S, Arendt W, Schmidt V (2009) Simulating the formation of keratin filament networks by a piecewise-deterministic Markov process. J Theor Biol 256:518-532
4. Bobick BE, Tuan RS, Chen FH (2010) The intermediate filament vimentin regulates chondrogenesis of adult human bone marrow-derived multipotent progenitor cells. J Cell Biochem 109:265–276
5. Couprie M, Bezerra FN, Bertrand G (2001) Topological operators for grayscale processing. J Electron Imaging 10:1003–1015
6. Canny J (1986) A computational approach to edge detection. IEEE T Pattern Anal 8:679–698
7. Daley DJ, Vere-Jones D (2003/08) An Introduction to the Theory of Point Processes. Volume I and II. Springer, New York.

8. Darling EM, Topel BS, Zauscher S, Vail TP, Guilak F (2008) Viscoelastic properties of mesenchymally-derived stem cells and primary osteoblasts, chondrocytes, and adipocytes. J Biomech 41:454–464
9. Deriche R (1987) Using Canny's criteria to derive a recursively implemented optimal edge detector. Int J Comput Vision 1:167–187
10. Docheva D, Padula D, Popov C, Mutschler W, Clausen-Schaumann H, Schieker M (2008) Researching into the cellular shape, volume and elasticity of mesenchymal stem cells, osteoblasts and osteosarcoma cells by atomic force microscopy. J Cell Mol Med 12:537-552
11. Dubochet J (2007) The physics of rapid cooling and its implications for cryoimmobilization of cells. Method Cell Biol 79:7-21
12. Eriksson JE, Dechat T, Grin B, Helfand B, Mendez M, Pallari HM, Goldman RD (2009) Introducing intermediate filaments: from discovery to disease. J Clin Invest 119:1763-1771
13. Fiedler J, Röderer G, Günther KP, Brenner R (2002) BMP-2, BMP-4, and PDGF-bb stimulate chemotactic migration of primary human mesenchymal progenitor cells. J Cell Biochem 87:305–312
14. Fiedler J, Leucht F, Waltenberger J, Dehio C, Brenner RE (2005) VEGF-A and PlGF-1 stimulate chemotactic migration of human mesenchymal progenitor cells. Biochem Biophys Res Commun 334:561-568
15. Fiedler J, Brill C, Blum WF, Brenner RE (2006) IGF-I and IGF-II stimulate directed cell migration of bone-marrow-derived human mesenchymal progenitor cells. Biochem Biophys Res Commun 345:1177–1183
16. Fleischer F, Ananthakrishnan R, Eckel S, Schmidt H, Käs J, Svitkina T, Schmidt V, Beil M (2007) Actin network architecture and elasticity in lamellipodia of melanoma cells. New J Phys 9:420
17. Hayter AJ (1984) A proof of the conjecture that the Tukey-Kramer multiple comparisons procedure is conservative. Ann Stat 12:61–75
18. Heussinger C, Frey E (2007) Role of architecture in the elastic response of semiflexible polymer and fiber networks. Phys Rev E 75:011917
19. Hohenberg HH, Müller-Reichert T, Schwarz H, Zierold K (2003) Foreword, special issue on high pressure freezing. J Microsc 212:1-2
20. Huisman EM, van Dillen TM, Onck PR, Van der Giessen E (2007) Three-dimensional cross-linked F-actin networks: Relation between network architecture and mechanical behavior. Phys Rev Lett 99:208103
21. Jackson WM, Jaasma MJ, Tang RY, Keaveny TM (2008) Mechanical loading by fluid shear is sufficient to alter the cytoskeletal composition of osteoblastic cells. Am J Cell Physiol 295:C1007–C1015
22. Janmey PA, Euteneuer U, Traub P, Schliwa M (1991) Viscoelastic properties of vimentin compared with other filamentous biopolymer networks. J Cell Biol 113:155-160
23. Joos H, Albrecht W, Laufer S, Reichel H, Brenner RE (2008) IL-1beta regulates FHL2 and other cytoskeleton-related genes in human chondrocytes. Mol Med 150-159
24. Kramer CY (1956) Extension of multiple range tests to group means with unequal numbers of replications. Biometrics 12:307–310
25. Kreplak L, Bär H, Leterrier JF, Herrmann H, Aebi U (2005) Exploring the mechanical behavior of single intermediate filaments. J Mol Biol 354:569-577
26. Landini G (2010) ImageJ plugins and macros http://www.dentistry.bham.ac.uk/landinig/software/software.html
27. Lin Y, Broedersz CP, Rowat AC, Wedig T, Herrmann H, MacKintosh FC, Weitz DA (2010) Divalent cations crosslink vimentin intermediate filament tail domains to regulate network mechanics. J Mol Biol 399:637–644
28. Lück S, Sailer M, Schmidt V, Walther P (2010) Three-dimensional analysis of intermediate filament networks using SEM-tomography. J Microsc 239:1–16
29. MacKintosh F, Käs J, Janmey PA (1995) Elasticity of semiflexible biopolymer networks. Phys Rev Lett 75:4425-4428
30. Mayer J, Schmidt V, Schweiggert F (2004) A unified simulation framework for spatial stochastic models. Simul Model Pract Th 12:307–326
31. Mayr-Wohlfart U, Waltenberger J, Hausser H, Kessler S, Gunther KP, Dehio C, Puhl W, Brenner RE (2002) Vascular endothelial growth factor stimulates chemotactic migration of primary human osteoblasts. Bone 30:472–477

32. Mücke N, Kreplak L, Kirmse R, Wedig T, Herrmann H, Aebi U, Langowski J (2004) Assessing the flexibility of intermediate filaments by atomic force microscopy. J Mol Biol 335:1241-1250
33. Mücke N, Kirmse R, Wedig T, Leterrier JF, Kreplak L (2005) Investigation of the morphology of intermediate filaments adsorbed to different solid supports. J Struct Biol 150:268–276
34. Nakasaki M, Yoshioka K, Miyamoto Y, Sasaki T, Yoshikawa H, Itoh K (2008) IGF-I secreted by osteoblasts acts as a potent chemotactic factor for osteoblasts. Bone 43:869-879
35. Ozkucur N, Monsees TK, Perike S, Do HQ, Funk RH (2009) Local calcium elevation and cell elongation initiate guided motility in electrically stimulated osteoblast-like cells. PLoS One 4:e6131
36. O'Neill GM (2009) The coordination between actin filaments and adhesion in mesenchymal migration. Cell Adh Migr 3:355–357
37. Rasband WS (1997-2010) ImageJ. U.S. National Institutes of Health, Bethesda, Maryland, USA
http://rsb.info.nih.gov/ij/
38. Resch GP, Goldie KN, Krebs A, Hoenger A, Small JV (2002) Visualisation of the actin cytoskeleton by cryo-electron microscopy. J Cell Sci 115:1877–1882
39. Ris H (1985) The cytoplasmic filament system in critical point-dried whole mounts and plastic-embedded sections. J Cell Biol 100, 1474–1487
40. Rodríguez JP, González M, Ríos S, Cambiazo V (2004) Cytoskeletal organization of human mesenchymal stem cells (MSC) changes during their osteogenic differentiation. J Cell Biochem 93:721-731
41. Sailer M, Höhn K, Lück S, Schmidt V, Beil M, Walther P (2010) Novel electron tomographic methods to study the morphology of keratin filament networks. Microsc Microanal 16:462–471
42. Schopferer M, Bar, H, Hochstein B, Sharma S, Mucke N, Herrmann H, Willenbacher N (2009). Desmin and vimentin intermediate filament networks: their viscoelastic properties investigated by mechanical rheometry. J Mol Biol 388:133-143
43. Stoyan D, Stoyan H (1994) Fractals, Random Shapes and Point Fields. Methods of Geometrical Statistics. Wiley, Chichester.
44. Trickey WR, Vail TP, Guilak F (2004) The role of the cytoskeleton in the viscoelastic properties of human articular chondrocytes. J Orthop Res 22:131-139
45. Treiser MD, Yang EH, Gordonov S, Cohen DM, Androulakis IP, Kohn J, Chen CS, Moghe PV (2010) Cytoskeleton-based forecasting of stem cell lineage fates. P Natl Acad Sci USA 12:610–615
46. Urban E, Jacob S, Nemethova M, Resch GP, Small JV (2010) Electron tomography reveals unbranched networks of actin filaments in lamellipodia. Nat Cell Biol 12:429–435
47. Vignal E, Resch G (2003) Shedding light and electrons on the lamellipodium: imaging the motor of crawling cells. Biotechniques 34:780-784, 786:788-789
48. Weichsel J, Herold N, Lehmann MJ, Kräusslich H, Schwarz US (2010) A quantitative measure for alterations in the actin cytoskeleton investigated with automated high-throughput microscopy. Cytom Part A 77A:52–63
49. Windoffer R, Woll S, Strnad P, Leube RE (2004) Identification of novel principles of keratin filament network turnover in living cells. Mol Biol Cell 15:2436-2448
50. Yourek G, Hussain MA, Mao JJ (2007) Cytoskeletal changes of mesenchymal stem cells during differentiation. ASAIO J 53:219–228